

# Selective photoelectrochemical synthesis of adipic acid using single-atom Ir decorated $\alpha$ -Fe<sub>2</sub>O<sub>3</sub> photoanode

Received: 17 January 2025

Accepted: 27 May 2025

Published online: 02 June 2025



Shenghe Si<sup>1,2,5</sup>, Yuyin Mao<sup>3,5</sup>, Ying-Ao Liu<sup>1,2</sup>, Jun Ma<sup>1,2</sup>, Weiyi Jiang<sup>4</sup>, En-Dian Zhao<sup>1,2</sup>, Kepeng Song<sup>1,2</sup>, Hefeng Cheng<sup>1,2</sup>✉, Baibiao Huang<sup>3</sup>, Dong Liu<sup>1,2</sup>✉ & Yujie Xiong<sup>1,2</sup>✉

Photoelectrochemical (PEC) synthesis offers a sustainable route for fine chemicals production, yet comprehending and modulating the reaction processes at the atomic level remains a challenge. Herein, we develop a single-atom Ir decorated Ti-doped  $\alpha$ -Fe<sub>2</sub>O<sub>3</sub> photoanode for selective PEC synthesis of adipic acid from cyclohexanone using water as the oxygen source. The PEC system achieves 6.0  $\mu\text{mol cm}^{-2} \text{h}^{-1}$  adipic acid production with ~60% Faradaic efficiency and ~88% selectivity. The single-atom Ir promotes the photogenerated carrier separation and transfer, while regulating the electronic structure of Ti-doped  $\alpha$ -Fe<sub>2</sub>O<sub>3</sub> photoanode to optimize its adsorption strength of OH<sup>-</sup> and cyclohexanone. Mechanistic studies reveal a non-free-radical reaction pathway at the atomic level, driven by photogenerated holes through an adsorbed hydroxyl transfer. Notably, integrating the photoanode and an amorphous silicon-based photocathode leads to a bias-free PEC device that enables stable adipic acid production for over 80 hours, underscoring the potential for sustainable light-driven synthesis.

Selective and energy-efficient synthesis of value-added chemicals is crucial for chemical manufacturing. Photoelectrochemical (PEC) technique represents a sustainable approach to solar-to-chemical energy conversion<sup>1–3</sup>. In addition to its established applications in water splitting and CO<sub>2</sub> reduction, PEC technique has also shown immense promise in biomass upgrading<sup>4</sup>, pharmaceutical intermediate synthesis<sup>5</sup>, and fine chemicals production<sup>6,7</sup>. This adaptability can be attributed to its capacity to synergistically integrate photo- and electrochemical processes, allowing the precise modulation of chemical reactions<sup>8,9</sup>. For instance, BiVO<sub>4</sub> photoanode exhibits remarkable performance in the PEC selective oxidation of biomass-derived glycerol to dihydroxyacetone, a compound widely used in cosmetic, pharmaceutical and

fine chemicals<sup>10–12</sup>. Similarly, Mo-doped WO<sub>3</sub> photoanode has been demonstrated to effectively promote PEC decarboxylative trifluoromethylation, which is critical for the modification of pharmaceutical and agrochemical compounds. Notably, this technique facilitates 100-gram-scale synthesis using PEC flow cells, indicating its potential for practical applications<sup>5</sup>. Despite such advancements, the intricacy of photoelectrode surface structures and radical-dominated mechanisms highlights a notable deficiency in comprehending and modulating the reaction process at the atomic level.

Single-atom catalysts (SACs) have emerged as one prominent candidate for heterogeneous catalysis due to their uniform chemical environment, distinctive electronic structure, high catalytic activity,

<sup>1</sup>School of Chemistry and Materials Science, University of Science and Technology of China, Hefei, Anhui, China. <sup>2</sup>State Key Laboratory of Bioinspired Interfacial Materials Science, Sustainable Energy and Environmental Materials Innovation Center, School of Nano Science and Technology, Suzhou Institute for Advanced Research, University of Science and Technology of China, Suzhou, Jiangsu, China. <sup>3</sup>State Key Laboratory of Crystal Materials, Institute of Crystal Materials, School of Chemistry and Chemical Engineering, Shandong University, Jinan, China. <sup>4</sup>Institute of Technology for Carbon Neutrality, College of Environmental Science and Engineering, Yangzhou University, Yangzhou, China. <sup>5</sup>These authors contributed equally: Shenghe Si, Yuyin Mao.

✉ e-mail: [chenghefeng@sdu.edu.cn](mailto:chenghefeng@sdu.edu.cn); [dongliu@ustc.edu.cn](mailto:dongliu@ustc.edu.cn); [yjxiong@ustc.edu.cn](mailto:yjxiong@ustc.edu.cn)

and high atom utilization<sup>13–15</sup>. These attributes make SACs an ideal model for addressing the aforementioned challenges in PEC systems. Only recently, engineering SACs has been progressively employed to enhance the performance of PEC water splitting<sup>16,17</sup>. This SACs-engineering approach has proven effective in promoting the separation and transfer of photogenerated carriers, while also reducing the reaction barrier as a specific water oxidation active site<sup>18–20</sup>. As a result, the photoelectrodes engineered with single-atom sites exhibit elevated photocurrent densities and enhanced solar-to-hydrogen (STH) efficiency. Recent studies on PEC alcohols and aldehydes oxidation as alternatives to water oxidation also demonstrate the beneficial effects of single atoms on photogenerated charge kinetics and free radicals generation<sup>21,22</sup>. Hydroxyl radicals ( $\cdot\text{OH}$ ) are typically regarded as the reactive oxygen species in such systems. Nevertheless, it remains unclear whether single-atom sites primarily act as adsorption sites for reactants or as active sites for reactive species generation. Moreover, the mechanisms underlying the synergistic effects of single-atom sites and photoelectrode surfaces during catalysis remains elusive.

Herein, we present a PEC strategy for the selective synthesis of adipic acid (AA), a crucial raw material for the manufacture of polyesters, polyamides, lubricants and plasticisers<sup>23</sup>, on single-atom active sites decorated Ti-doped  $\alpha\text{-Fe}_2\text{O}_3$  photoanode. Industrially, AA is produced via catalytic oxidation of the cyclohexanol/cyclohexanone mixture (KA oil) in concentrated nitric acid, which is energy-intensive and gives rise to serious environmental issues such as  $\text{N}_2\text{O}$  emission<sup>24</sup>. To avoid the  $\text{N}_2\text{O}$  emission, the catalytic dehydroxylation and hydrogenation approach has been developed for converting glucaric acid to obtain AA<sup>25–27</sup>. However, the ring-opening reaction and the selective oxidation of cyclohexanone or cyclohexanol under mild conditions impose significant challenges<sup>28,29</sup>, especially in an efficient PEC system with sustainable solar energy. To this end, in this work we establish a selective PEC synthesis of AA via cyclohexanone oxidation using a single-atom Ir decorated Ti-doped  $\alpha\text{-Fe}_2\text{O}_3$  photoanode, where water serves as the sole oxygen source and light-coupled electrical bias provides the energy input. The incorporation of Ir single atoms not only promotes the separation and transfer of photogenerated carriers, but also enhances the adsorption and conversion of cyclohexanone. At 1.5 V versus reversible hydrogen electrode (vs. RHE), the as-prepared photoanode achieves an AA production rate of  $6\ \mu\text{mol cm}^{-2}\text{ h}^{-1}$  with ~60% Faradaic efficiency (FE) and ~88% selectivity. Moreover, combined in situ spectroscopy and detailed experiments resolve a non-free-radical reaction mechanism for selective oxidation of cyclohexanone to AA, which is driven by photogenerated holes and synergizes adsorbed hydroxyl ( $\cdot\text{OH}$ ) transfer on the as-prepared photoanode surface. Theoretical calculations demonstrate that Ir single atoms strongly adsorb  $\text{OH}^-$  and regulate the electronic structure of  $\alpha\text{-Fe}_2\text{O}_3$  to promote adsorption of cyclohexanone at Fe sites, thereby balancing the competing adsorption of cyclohexanone and  $\text{OH}^-$ . Finally, we design and construct an integrated system consisting of the single-atom sites engineered photoanode and an amorphous silicon-based (a-Si) photocathode. This unassisted SACs-based PEC system demonstrates selective, stable and efficient AA production, illustrating the promise of single-atom catalysis for sustainable chemical manufacturing.

## Results and discussion

### Synthesis and characterizations

Figure 1a illustrates the synthetic procedure of single-atom Ir decorated  $\alpha\text{-Fe}_2\text{O}_3$  photoanode (see details in Experimental section). To improve the conductivity and photocurrent density of  $\alpha\text{-Fe}_2\text{O}_3$  photoanode, Ti doping strategy<sup>30,31</sup> was adopted in this work, and thus leads to Ti-doped  $\alpha\text{-Fe}_2\text{O}_3$  (TFO) as the model photoanode. Specifically, TFO were grown on fluorine-doped tin oxide (FTO) glass substrates via hydrothermal method followed by annealing in air. Subsequently, electrochemical deposition treatment was carried out

to prepare the single-atom Ir decorated TFO sample ( $\text{Ir}_1/\text{TFO}$ ). For comparison,  $\text{IrO}_x$  clusters decorated TFO sample ( $\text{IrO}_x/\text{TFO}$ ) was also prepared via electrochemical deposition. As shown in the X-ray diffraction (XRD) patterns (Supplementary Fig. 1), TFO,  $\text{Ir}_1/\text{TFO}$  and  $\text{IrO}_x/\text{TFO}$  samples exhibit the hematite phase (JCPDS No. 33-0664). Scanning electron microscopy (SEM) and transmission electron microscopy (TEM) images confirm that all samples possess nanorods structure (Supplementary Fig. 2a–c, Fig. 1b, Supplementary Fig. 3 and Supplementary Fig. 4a–c). From the aberration-corrected high-angle annular dark-field scanning transmission electron microscopy (AC-HAADF-STEM, Fig. 1c) image, the observed interplanar distance of 0.27 nm corresponds well to the (104) plane of hematite<sup>32</sup>, and no Ir-related nanoparticles are found on the surface of  $\text{Ir}_1/\text{TFO}$ . Similar structures were also observed in the high-resolution TEM (HRTEM) images of TFO and  $\text{IrO}_x/\text{TFO}$  (Supplementary Figs. 2d, 4d). Furthermore, as the contrast of the atomic columns is approximately proportional to the square of the atomic number ( $Z$ )<sup>33</sup>, the bright spots marked with yellow circles are identified as Ir single atoms, as confirmed by the corresponding strength line profiles (Fig. 1d). Additionally, energy-dispersive X-ray spectroscopy (EDS) elemental mapping also displays the uniform distribution of Ir and Ti elements on  $\text{Ir}_1/\text{TFO}$  sample (Fig. 1e). For  $\text{IrO}_x/\text{TFO}$  sample, distinct  $\text{IrO}_x$  clusters with a diameter of 1–2 nm can be observed (Supplementary Fig. 4e, f).

To investigate the electronic structure and local coordination environment of the above samples, we conducted X-ray photoelectron spectroscopy and X-ray absorption fine spectroscopy (XAFS). The Fe 2p spectra (Supplementary Fig. 5a) exhibit the spin-orbit coupling splitting, which is a featured characteristic of  $\text{Fe}_2\text{O}_3$  sample<sup>34</sup>. The O 1s spectra can be cleaved into lattice oxygen, oxygen vacancy and hydroxyl peaks (Supplementary Fig. 5b)<sup>35</sup>. It is observed that the incorporation of Ir single atoms has negligible effect on the O 1s orbitals. In contrast, introducing  $\text{IrO}_x$  clusters shifts the lattice oxygen peak to lower binding energy, indicating the presence of substantial Ir–O interaction. The two peaks observed in the Ti 2p spectra are attributed to the Ti 2p<sub>3/2</sub> and Ti 2p<sub>1/2</sub> orbitals of Ti<sup>4+</sup>, respectively, which corroborates the successful doping of Ti<sup>4+</sup> in the samples (Supplementary Fig. 5c). Importantly, the binding energies of Ir 4f<sub>7/2</sub> and Ir 4f<sub>5/2</sub> in  $\text{Ir}_1/\text{TFO}$  sample are observed at 62.4 and 64.7 eV, respectively, proving the positive oxidation state of Ir single atoms (Fig. 2a)<sup>36</sup>. For the  $\text{IrO}_x/\text{TFO}$  sample, the Ir 4f spectrum shifts to higher binding energy, suggesting an oxidation state approaching +4. To further reveal the fine structure of Ir species, Ir L<sub>3</sub>-edge X-ray absorption near-edge structure (XANES) and extended X-ray absorption fine structure (EXAFS) analyses were carried out. As shown in Fig. 2b, the positions of white line peaks for  $\text{Ir}_1/\text{TFO}$  and  $\text{IrO}_x/\text{TFO}$  are close to that of  $\text{IrO}_2$  standard, suggesting that the oxidation state of Ir species are close to +4 (ref. 37). As depicted in Ir L<sub>3</sub>-edge EXAFS spectra (Fig. 2c), both  $\text{Ir}_1/\text{TFO}$  and  $\text{IrO}_x/\text{TFO}$  display one prominent peak at about 1.6 Å, which can be attributed to the Ir–O coordination.

EXAFS spectra (Fig. 2c), both  $\text{Ir}_1/\text{TFO}$  and  $\text{IrO}_x/\text{TFO}$  display one prominent peak at about 1.6 Å, which can be attributed to the Ir–O coordination. The absence of Ir–Ir (~2.6 Å) and Ir–O–Ir (~3.5 Å) bonds in the  $\text{Ir}_1/\text{TFO}$  sample, contrasted with the presence of Ir–O–Ir bonds in the  $\text{IrO}_x/\text{TFO}$  sample, confirms the successful introduction of Ir single atoms and  $\text{IrO}_x$  clusters, respectively. The experimental Ir L<sub>3</sub>-edge EXAFS spectra were further fitted to give their corresponding local coordination structures (Fig. 2d, e, Supplementary Fig. 6a, b and Supplementary Table 1). The fitting results suggest that each Ir single atom is coordinated to five oxygen atoms in  $\text{Ir}_1/\text{TFO}$  sample (Fig. 2d), which is different from the saturated six coordination state of Ir atoms in  $\text{IrO}_x/\text{TFO}$  sample (Fig. 2e).

UV–vis diffuse reflectance spectra of TFO,  $\text{Ir}_1/\text{TFO}$  and  $\text{IrO}_x/\text{TFO}$  samples exhibit similar absorption edge at 605–610 nm (Supplementary Fig. 7a), indicating that the introduction of Ir species does not alter the light adsorption of TFO samples. Tauc plots (Supplementary Fig. 7b)

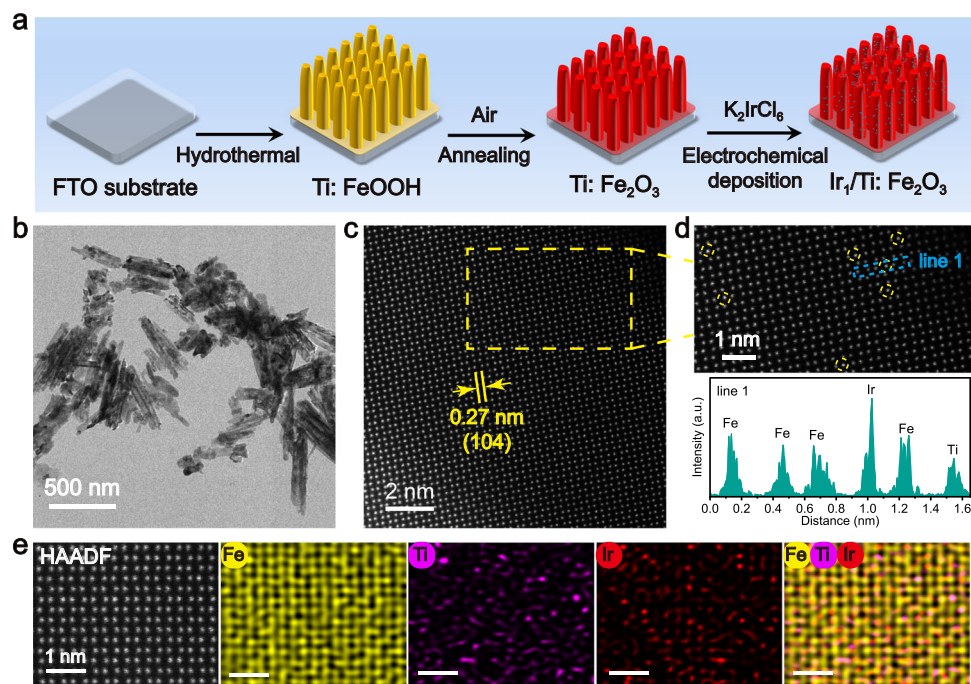


**Fig. 1 | Fabrication and morphological characterizations of Ir<sub>1</sub>/TFO.** **a** Schematic illustration for the synthesis of Ir<sub>1</sub>/TFO. **b** TEM image of Ir<sub>1</sub>/TFO. **c** AC-STEM-HAADF image of Ir<sub>1</sub>/TFO. **d** Magnified AC-HAADF-STEM image of Ir<sub>1</sub>/TFO and the corresponding strength line profiles. **e** EDS elemental mappings of Ir<sub>1</sub>/TFO.

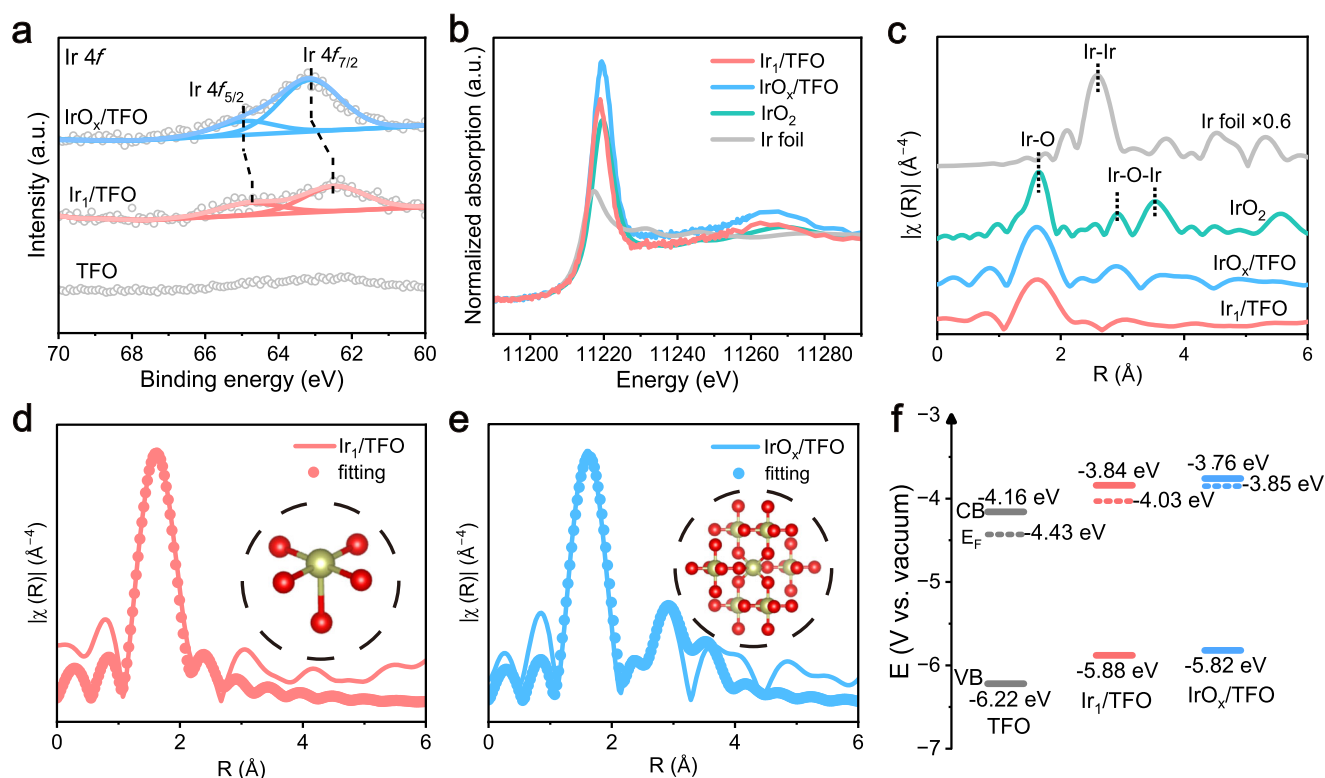


**Fig. 2 | Structural information of the samples.** **a** XPS spectra of Ir 4f for different samples. Ir  $L_{3-}$  edge XANES spectra (**b**) and Fourier transformed EXAFS spectra (**c**) of Ir foil, IrO<sub>2</sub>, Ir<sub>1</sub>/TFO and IrO<sub>x</sub>/TFO. EXAFS fitting curves of Ir<sub>1</sub>/TFO (**d**) and IrO<sub>x</sub>/TFO

(**e**) at the R space. Insets: corresponding possible structural models. **f** Band structures of TFO, Ir<sub>1</sub>/TFO and IrO<sub>x</sub>/TFO samples.

and UV photoelectron spectroscopy (UPS) were used to determine their band structures (Supplementary Fig. 8), including Fermi level ( $E_F$ ), valence band maximum (VBM), and conduction band minimum (CBM), as illustrated in Fig. 2f. Both Ir<sub>1</sub>/TFO and IrO<sub>x</sub>/TFO samples present

upward shift relative to the bare TFO sample. The upward shift of band level is typically advantageous for achieving a more favorable band bending at the photoelectrodes/electrolytes interface, which can in turn facilitate more efficient photogenerated carrier separation<sup>11</sup>.

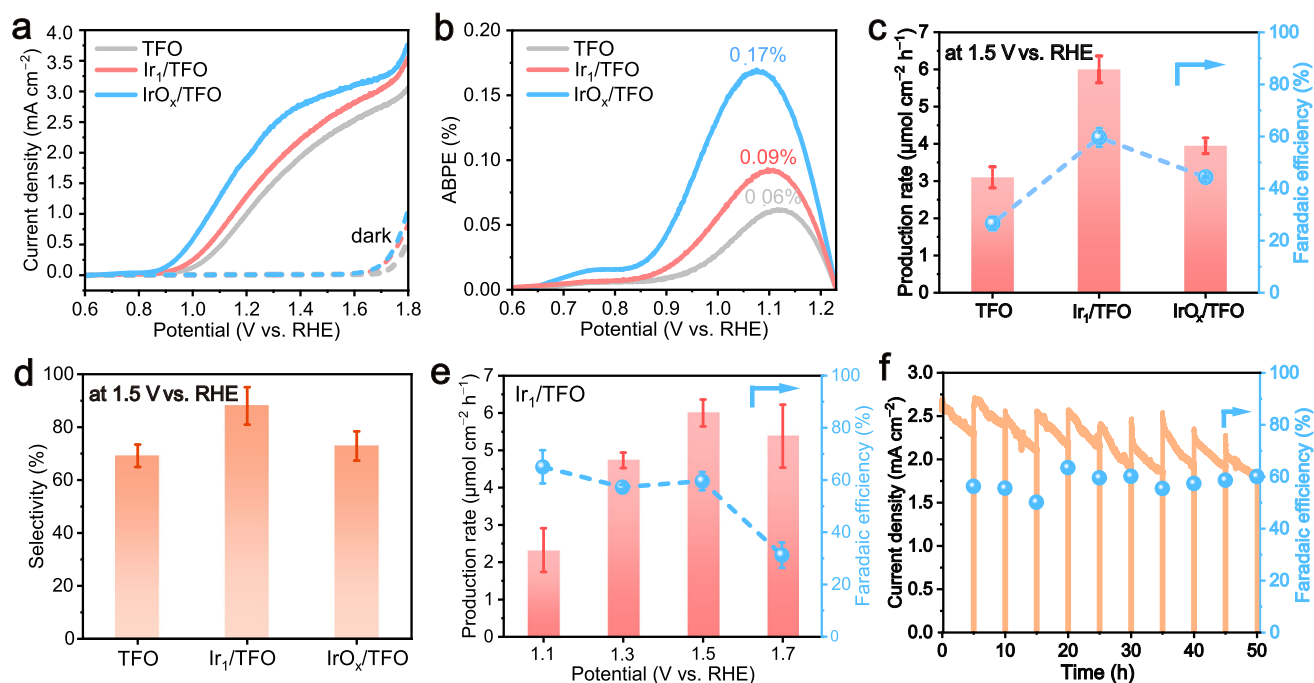


**Fig. 3 | PEC performance for cyclohexanone conversion.** LSV curves (a) and ABPE values (b) of TFO, Ir<sub>1</sub>/TFO and IrO<sub>x</sub>/TFO photoanodes in 1 M KOH without cyclohexanone under AM 1.5 G (100 mWcm<sup>-2</sup>) illumination. c PEC cyclohexanone oxidation performance over TFO, Ir<sub>1</sub>/TFO and IrO<sub>x</sub>/TFO photoanodes at 1.5 V vs. RHE in 1 M KOH with 20 mM cyclohexanone under AM 1.5 G (100 mWcm<sup>-2</sup>) illumination.

### PEC performance and charge kinetics analysis

Figure 3a shows linear sweep voltammetry (LSV) curves of the photoanodes in 1 M KOH electrolyte under AM 1.5 G simulated sunlight (100 mW cm<sup>-2</sup>). The bare TFO photoanode displays a photocurrent density of 1.16 mA cm<sup>-2</sup> at 1.23 V vs. RHE with an onset potential ( $V_{\text{onset}}$ ) of 0.94 V. The incorporation of Ir species enhances photocurrent densities of both Ir<sub>1</sub>/TFO and IrO<sub>x</sub>/TFO photoanodes, accompanied by the negative shifts of  $V_{\text{on}}$ . This indicates that the addition of Ir species, particularly IrO<sub>x</sub>, facilitates photogenerated carrier transfer and reduces the overpotential of water oxidation. Figure 3b illustrates the enhanced value of the applied bias photo-to-current efficiency (ABPE) for the Ir<sub>1</sub>/TFO and IrO<sub>x</sub>/TFO photoanodes, which are observed to be 0.09% and 0.17%, respectively. To evaluate the charge injection efficiency ( $\eta_{\text{inj}}$ ) and charge separation efficiency ( $\eta_{\text{sep}}$ ), we measured the PEC performance of these samples in the electrolyte with 0.5 M NaSO<sub>3</sub> (Supplementary Fig. 9a–c). The obtained  $\eta_{\text{inj}}$  values at 1.23 V vs. RHE follow the order: IrO<sub>x</sub>/TFO (61.0%) > Ir<sub>1</sub>/TFO (46.1%) > TFO (43.4%), indicating that Ir species enhance surface holes trapping and facilitate water oxidation (Supplementary Fig. 9d–f). Combined with the theoretical current density ( $J_{\text{abs}}$ ), both Ir<sub>1</sub>/TFO and IrO<sub>x</sub>/TFO exhibit higher  $\eta_{\text{sep}}$  compared to TFO, indicating that efficient holes transport from the bulk to the surface owing to the incorporation of Ir species<sup>19</sup>. Besides, small discrepancies between steady-state and transient photocurrent density can be achieved on the Ir<sub>1</sub>/TFO and IrO<sub>x</sub>/TFO photoanodes (Supplementary Fig. 10), implying promoted water oxidation by Ir species and subdued photogenerated carrier recombination<sup>38</sup>. Subsequently, normalized open circuit potential (OCP) decay curves further reveal faster OCP decay for Ir<sub>1</sub>/TFO and IrO<sub>x</sub>/TFO photoanodes (Supplementary Fig. 11a), suggesting improved photogenerated carrier separation and shorter carrier transfer lifetimes ( $\tau$ ), as calculated based on the derived-OCP values (Supplementary Fig. 11b). The results reveal that the striking built-in electric field between the bulk and surface created by Ir species efficiently enhances photogenerated

carrier separation and transfer kinetics<sup>39</sup>. Moreover, steady-state photoluminescence (PL) spectra (Supplementary Fig. 12a), time-resolved photoluminescence (TRPL) spectra (Supplementary Fig. 12b and Supplementary Table 2) and photoelectrochemical impedance spectra (PEIS, Supplementary Fig. 12c) also demonstrate that the Ir species can significantly inhibit the photogenerated carrier recombination, while simultaneously promote carrier separation and transfer.

### PEC cyclohexanone oxidation reaction

PEC cyclohexanone oxidation reactions were conducted in a sealed H-type photoelectrochemical cell (Supplementary Fig. 13). The addition of cyclohexanone to the electrolyte led to a slight increase in anodic current (Supplementary Fig. 14), particularly for the Ir<sub>1</sub>/TFO photoanode, indicating that the thermodynamic constraints of cyclohexanone oxidation are more favorable than those of the oxygen evolution reaction (OER). Moreover, the LSV results for Ir<sub>1</sub>/TFO photoanode in varying cyclohexanone concentrations indicate that mass transfer dominates PEC performance in the low-concentration range (0–50 mM, Supplementary Fig. 15). The oxidation products were identified and quantified using nuclear magnetic resonance (NMR) spectroscopy. We found that AA was the main oxidation product of cyclohexanone oxidation, with glutaric acid (GA) as the by-product (Supplementary Figs. 16–18). Figure 3c shows the production rate and FE of AA from PEC cyclohexanone oxidation over different photoanodes, and the corresponding I-t curves are displayed in Supplementary Fig. 19. The bare TFO photoanode exhibits a relatively low production rate (3.1 μmol cm<sup>-2</sup> h<sup>-1</sup>) and FE (26.6%) for cyclohexanone oxidation to AA. In contrast, the Ir<sub>1</sub>/TFO photoanode achieves the highest AA production rate (6.0 μmol cm<sup>-2</sup> h<sup>-1</sup>), with an FE of ~60% and highest selectivity reaching 88% (Fig. 3d). Although the IrO<sub>x</sub>/TFO photoanode generates the highest photocurrent, it exhibits inferior PEC performance in selective cyclohexanone oxidation to AA, with a production rate of 3.9 μmol cm<sup>-2</sup> h<sup>-1</sup> and a FE of 44.3%. In comparison,



$\text{IrO}_x$  clusters underperform in selective cyclohexanone oxidation due to their favorable reaction kinetics for water oxidation<sup>40,41</sup>. We further explored the PEC performance of cyclohexanone oxidation over  $\text{Ir}_1/\text{TFO}$  photoanode under different applied bias potentials (Fig. 3e). Within the range of 1.1–1.5 V vs. RHE, the production rate of AA increases with rising potential, while the FE of AA remains almost consistent. At 1.7 V vs. RHE, sufficient photogenerated holes drive the selective oxidation of cyclohexanone to AA with a slightly increased production rate. However, at higher potentials, excess photo-generated holes intensify the competing water oxidation leading to a declined FE. Furthermore, the effect of Ir loading (Supplementary Table 3) on the production rate and FE of AA was investigated (Supplementary Fig. 20). The results elucidate that in comparison with the agglomerated Ir species, the atomically-dispersed Ir species promote the selective cyclohexanone conversion, thereby enhancing the production rate, the selectivity and FE of AA. We also evaluated the performance of other cyclic ketones oxidation over  $\text{Ir}_1/\text{TFO}$  photoanode as shown in Supplementary Fig. 21. The  $\text{Ir}_1/\text{TFO}$  photoanode demonstrates appropriate versatility by enabling PEC oxidation of cyclic ketones to the corresponding dicarboxylic acids. However, the  $\text{Ir}_1/\text{TFO}$  photoanode exhibits suboptimal performance in the PEC oxidation of other cyclic ketones in comparison to PEC cyclohexanone oxidation. This discrepancy may be attributed to the solubility of the substrates in the electrolyte.

The  $\text{Ir}_1/\text{TFO}$  photoanode exhibits a distinctive benefit in selective cyclohexanone oxidation (Supplementary Fig. 22). In contrast with the electrocatalytic (EC) and photocatalytic (PC) reaction processes, our PEC system exhibits its unique advantages on catalytic performance (Supplementary Fig. 23). To achieve the comparable current density, an additional 0.35 V is required to apply on the cell without 100  $\text{mW cm}^{-2}$  light illumination. The production rate and FE of AA in electrocatalytic cyclohexanone oxidation are both markedly lower than those in PEC system. These results also demonstrate that the photogenerated carriers are essential for the PEC cyclohexanone oxidation. Additionally, we measured and calculated quantum efficiency (QE) of AA over  $\text{Ir}_1/\text{TFO}$  photoanode to evaluate the incident photon-to-AA conversion efficiency (Supplementary Fig. 24). A 14.8% incident photon-to-AA conversion efficiency can be achieved at a wavelength of 380 nm.

We also evaluated the long-term stability of the photoelectrode, which is critical for determining their suitability towards practical applications. As shown in Supplementary Fig. 25a, the photocurrent density of  $\text{Ir}_1/\text{TFO}$  could be relatively stable during continuous operation for 24 h. However, this stable photocurrent density does not mean stable AA production. A decline in the FE for AA could be observed (Supplementary Fig. 25b), which can be ascribed to a notable reduction in cyclohexanone concentration in the vicinity of the photoanode surface. Accordingly, we performed continuous cycling tests on  $\text{Ir}_1/\text{TFO}$  photoanode with supplying sufficient cyclohexanone for each cycle (Fig. 3f). Under the circumstances the photocurrent density together with the AA production of the  $\text{Ir}_1/\text{TFO}$  photoanode maintain stable over 10 cycles for more than 50 h. This system exhibits consistent photocurrent density and achieves high FEs of  $57.7 \pm 3.6\%$  for AA production, which indicates the good stability of  $\text{Ir}_1/\text{TFO}$  for PEC cyclohexanone oxidation. Additionally, cyclohexanol can be directly converted to cyclohexanone and AA in the PEC system (Supplementary Fig. 26). Then, when using commercial KA oil as the reactant, the  $\text{Ir}_1/\text{TFO}$  photoanode could produce AA at a production rate of  $2.65 \mu\text{mol cm}^{-2} \text{h}^{-1}$  (Supplementary Fig. 27), demonstrating its potential for practical applications.

### Insight into reaction mechanism

To identify the oxygen source in AA production, we conducted isotope-labeling experiments using 1 M KOH containing 10%  $\text{H}_2^{18}\text{O}$  as the electrolyte (Supplementary Fig. 28). The liquid chromatography mass

spectrometry (LC-MS) results display that  $^{18}\text{O}$  can be detected in AA production in the form of  $\text{C}_6\text{H}_9\text{O}_3^{18}\text{O}^-$ ,  $\text{C}_6\text{H}_9\text{O}_2^{18}\text{O}_2^-$  and  $\text{C}_6\text{H}_9^{18}\text{O}_3^-$  (Supplementary Fig. 28b), indicating that  $\text{H}_2\text{O}$  serves as the oxygen source for the PEC cyclohexanone oxidation to produce AA. As abovementioned, we have investigated the beneficial role of Ir single atoms in promoting photogenerated carrier separation and transfer. To ascertain the role of Ir single atoms in the specific cyclohexanone oxidation reaction, we firstly evaluated the adsorption behavior of cyclohexanone. The OCP was monitored at the photoanodes before and after the addition of cyclohexanone into the electrolyte (Supplementary Fig. 29), which could reflect the variation of absorbates in the Helmholtz layer<sup>42</sup>. When injecting cyclohexanone, a significant decrease in the OCP of  $\text{Ir}_1/\text{TFO}$  photoanode is observed, indicating pronounced adsorption, while the  $\text{IrO}_x/\text{TFO}$  and TFO photoanodes exhibit weaker adsorption<sup>43</sup>. To shield the active surfaces and catalytic sites,  $\text{Al}_2\text{O}_3$  passivated layer was coated on  $\text{Ir}_1/\text{TFO}$  photoanode via chemical bath deposition<sup>44</sup>. Both  $\text{Al}_2\text{O}_3$ -coated  $\text{Ir}_1/\text{TFO}$  surface (denoted as  $\text{Al}_2\text{O}_3/\text{Ir}_1/\text{TFO}$ ) and Ir single atoms decorated  $\text{Al}_2\text{O}_3$ -coated TFO surface (denoted as  $\text{Ir}_1/\text{Al}_2\text{O}_3/\text{TFO}$ ) exhibit a sharp decrease in AA production (Supplementary Fig. 30). This implies that the  $\text{Ir}_1\text{-Fe}_2\text{O}_3$  interface plays a pivotal role in the effective production of AA. We conducted in situ Raman spectroscopy to investigate the dynamic evolution of  $\text{Ir}_1/\text{TFO}$  photoanode (Fig. 4a, b). Without cyclohexanone, a new band at  $660 \text{ cm}^{-1}$  is observed, corresponding to the disorder in the  $\text{Fe}_2\text{O}_3$  crystal lattice when the applied potential increases to 1.0 V vs. RHE<sup>45</sup>. This may be due to the Fe-OOH species obtained through coupling of  $\text{OH}^-$  and photogenerated holes by  $\text{Fe}^{\text{IV}}=\text{O}$  species<sup>46</sup>, where the  $\text{Fe}^{\text{IV}}=\text{O}$  species are attributed to the evolution of photogenerated holes trapped by the surface states of  $\alpha\text{-Fe}_2\text{O}_3$ <sup>6</sup>. The formation of Fe-OOH species is believed to result from the sustained formation of  $^*\text{OH}$  on the  $\text{Fe}_2\text{O}_3$  surface during water oxidation<sup>47,48</sup>. Distinctly, after the addition of cyclohexanone, the characteristic band of Fe-OOH species appears only at higher potentials (over 1.3 V vs. RHE) with lower signal intensity. These findings demonstrate that the adsorption and conversion of cyclohexanone directly competes with the water oxidation, which leads to Fe-OOH species formation. Efficient cyclohexanone oxidation can suppress the formation of Fe-OOH species. Furthermore, we employed in situ Fourier transform infrared spectroscopy (FTIR) to probe the reaction species on the photoanodes. Before the addition of cyclohexanone, in situ FTIR was carried out to explore  $\text{H}_2\text{O}$  activation on the photoanodes. For  $\text{Ir}_1/\text{TFO}$  (Fig. 4c), the O–H stretching mode ( $3643 \text{ cm}^{-1}$ ) of adsorbed water molecules ( $^*\text{H}_2\text{O}$ ) displays an obvious blue-shift with increasing applied potential (1.0–1.4 V vs. RHE), implying that  $^*\text{H}_2\text{O}$  is converted to  $^*\text{OH}$ <sup>49</sup>. In contrast, TFO exhibits negligible shift with the increasing applied potential (Supplementary Fig. 31a). The  $\nu$  (O–H) band signal of  $\text{IrO}_x/\text{TFO}$  reaches saturation at 0.8 V vs. RHE, accompanied by a slight red-shift due to rapid conversion of  $^*\text{OH}$  (Supplementary Fig. 31b)<sup>50</sup>. Upon cyclohexanone addition, the characteristic signals of cyclohexanone consumption (1188, 1234, 1280, 1309, and  $1600 \text{ cm}^{-1}$ ) and AA formation (1143 and  $1498 \text{ cm}^{-1}$ ) were also detected by in situ FTIR (Fig. 4d)<sup>23</sup>, indicating the selective conversion of cyclohexanone to AA. Correspondingly, we carried out the control reactions to explore the reaction path of cyclohexanone to AA. Several possible intermediates were added into the PEC reaction as reported in the available literature<sup>51,52</sup>. As shown in Supplementary Fig. 32, the results show that 2-hydroxycyclohexanone is an important intermediate for the selective cyclohexanone conversion to AA. Upon identification of the reaction intermediates, we conducted in situ electron paramagnetic resonance (EPR) spectroscopy to detect the free radicals in cyclohexanone oxidation where 5, 5-dimethyl-1-pyrroline-N-oxide (DMPO) served as the trapping agent (Fig. 4e). Using  $\text{Ir}_1/\text{TFO}$  as the photoanode, no signal was detected without applied potential in dark. In the absence of cyclohexanone in the PEC system, only hydroxyl radical ( $^*\text{OH}$ ) signals were detected, suggesting that the photo-generated holes produced by  $\text{Ir}_1/\text{TFO}$  are able to efficiently oxidize  $\text{OH}^-$

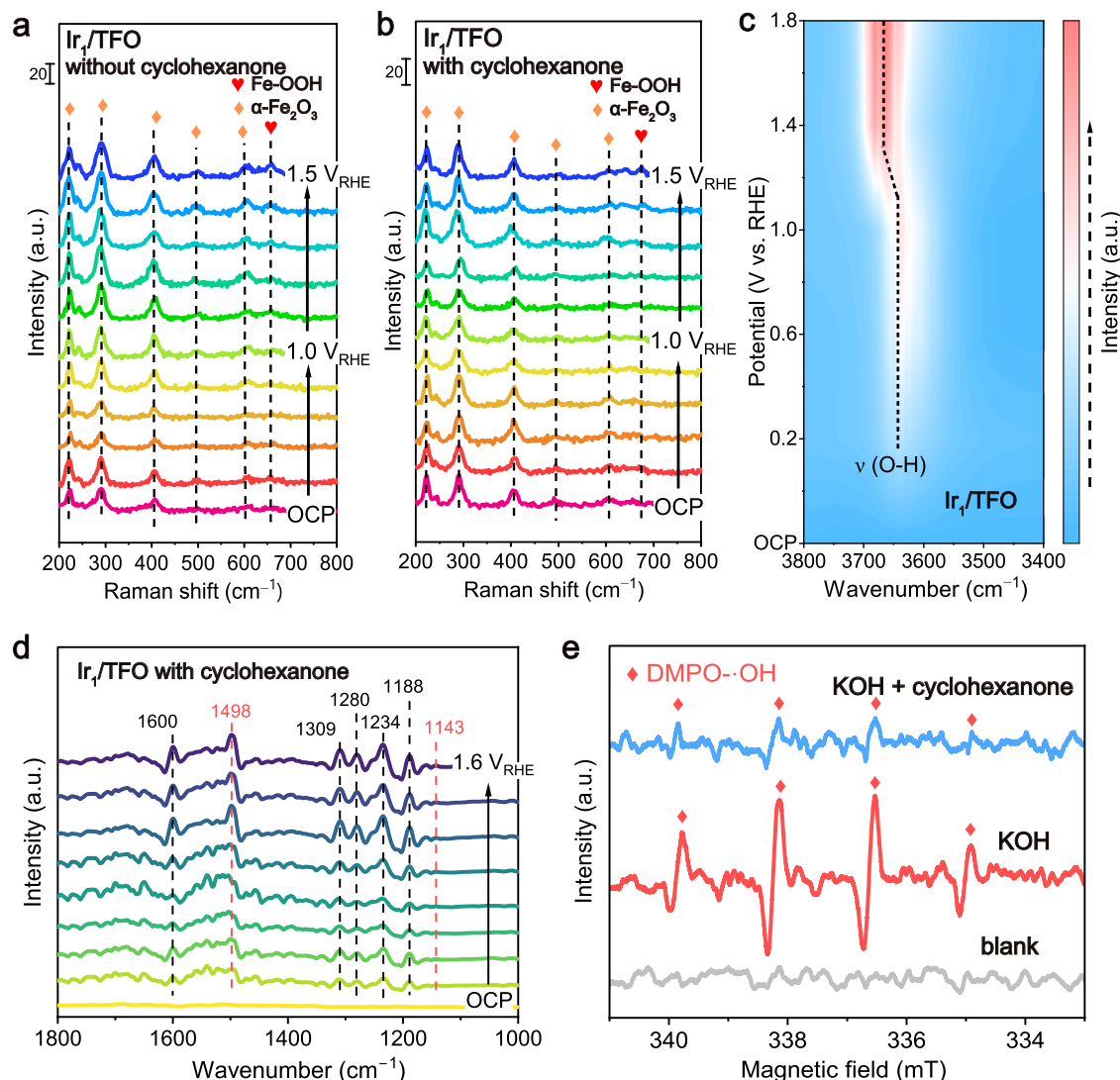


**Fig. 4 | In situ spectroscopy study of reaction mechanism.** In situ Raman spectra of the structural evolution on Ir<sub>1</sub>/TFO photoanode in PEC OER process (a) and in PEC cyclohexanone oxidation process (b). In situ FTIR spectra for PEC H<sub>2</sub>O

activation process (c) and PEC cyclohexanone oxidation process (d) on Ir<sub>1</sub>/TFO photoanode. e EPR signals over Ir<sub>1</sub>/TFO photoanode in 1 M KOH with and without cyclohexanone.

to •OH. The addition of cyclohexanone significantly reduces the •OH signal intensity, indicating that •OH formation is strongly inhibited. Notably, no carbon-centered radicals were detected in PEC cyclohexanone oxidation process. To further confirm the contribution of different active species to the PEC cyclohexanone oxidation, Na<sub>2</sub>SO<sub>3</sub>, tert-butanol (TBA) and NaIO<sub>3</sub> were added individually as photogenerated holes, •OH and photogenerated electrons scavengers, respectively (Supplementary Fig. 33). The addition of Na<sub>2</sub>SO<sub>3</sub> reduces AA production distinctly, while TBA has minimal effect, demonstrating that the PEC cyclohexanone oxidation process follows a photogenerated holes-induced oxidative mechanism involving •OH transfer, rather than the typical PEC organics oxidation induced by •OH radicals as reactive oxygen species<sup>53,54</sup>.

To further elucidate the role of Ir single atoms in this selective catalysis reaction, we carried out density functional theory (DFT) calculations. The structural models of bare TFO and Ir<sub>1</sub>/TFO are presented in Supplementary Fig. 34. To account for the existence of competitive adsorption of OH<sup>−</sup> and cyclohexanone, we calculated the adsorption energies of OH<sup>−</sup> and cyclohexanone on the surfaces of TFO and Ir<sub>1</sub>/TFO photoanodes, respectively. As shown in Fig. 5a, the adsorption strength of Fe site for •OH (−2.61 eV) is remarkably stronger than that

of cyclohexanone (−0.23 eV). With the introduction of single-atom Ir, the adsorption strength of Fe site for •OH and cyclohexanone is enhanced to −2.73 and −1.11 eV, respectively. The discrepancy in the adsorption strength of Fe site for •OH and cyclohexanone on the Ir<sub>1</sub>/TFO surface is reduced compared to that without cyclohexanone, whereas a considerable divergence remains on the Ir single-atom site (Fig. 5a). Briefly, OH<sup>−</sup> species prefer to bind with Ir single-atom site on the Ir<sub>1</sub>/TFO photoanode, and the presence of Ir single atom balances the competing adsorption of Fe site for OH<sup>−</sup> and cyclohexanone<sup>55</sup>. Charge density differences analysis demonstrates strong polarization between Ir single-atom site and •OH (Fig. 5b, c), thus facilitating the trapping and transfer of photogenerated holes. Partial density of states (PDOS) calculations of TFO and Ir<sub>1</sub>/TFO (Fig. 5d and Supplementary Fig. 35) indicate that the *d*-band center of Fe sites in Ir<sub>1</sub>/TFO is closer to the Fermi energy level than that of TFO, suggesting that Fe sites in Ir<sub>1</sub>/TFO feature more anti-bonding states, which enables robust *d-p* orbital interaction between Fe sites and cyclohexanone<sup>23</sup>. Combined with the DFT results and in situ experiments, Fig. 5e outlines the possible reaction path for the PEC selective oxidation of cyclohexanone to AA, which is driven by photogenerated holes and facilitated via •OH transfer at the atomic level. Specifically, photogenerated holes

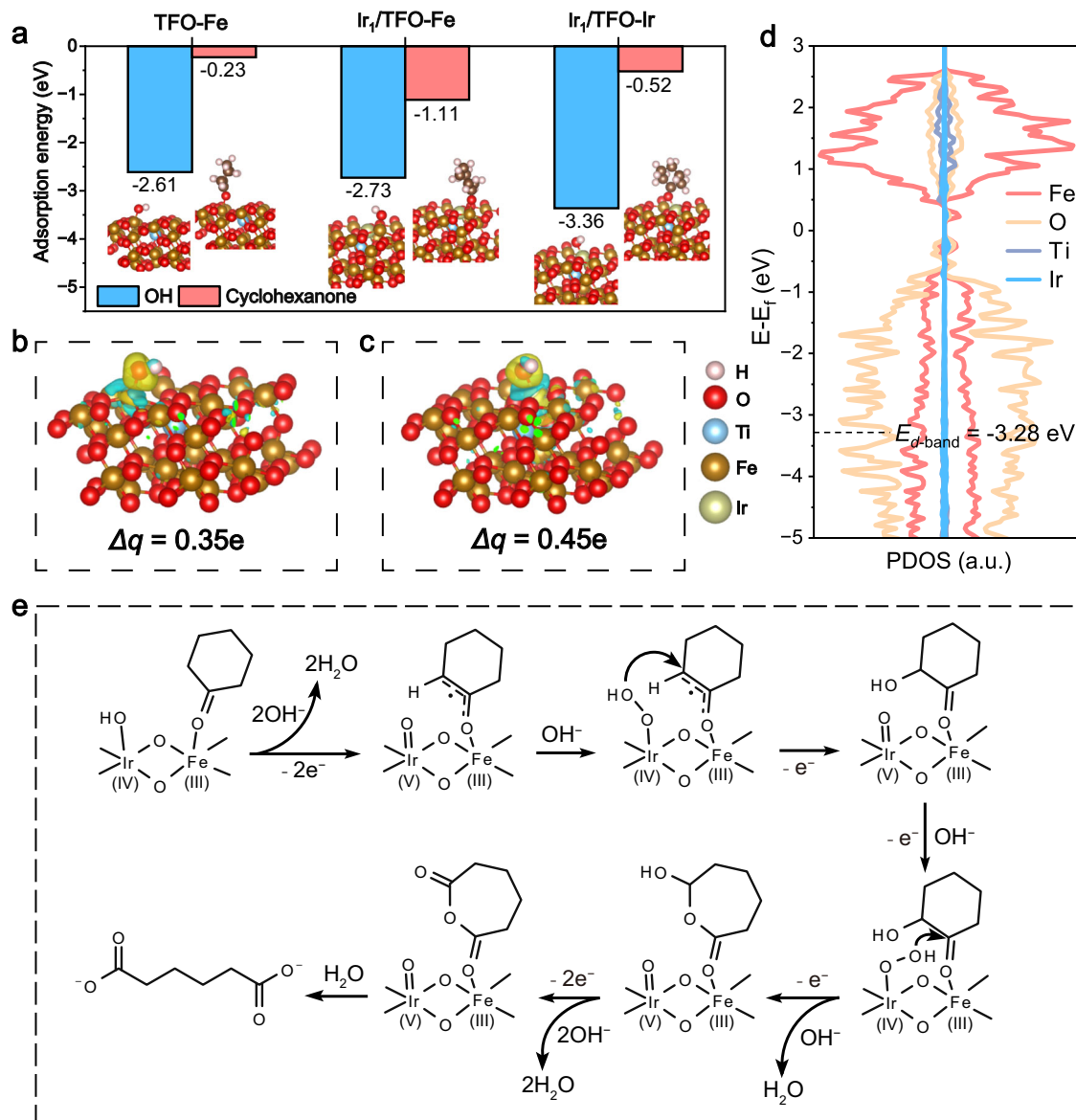


**Fig. 5 | DFT calculations and possible reaction process. a** Adsorption energies of OH⁻ and cyclohexanone over TFO and Ir₁/TFO. **b** Charge density difference between \*OH and Fe site over TFO. **c** Charge density difference between \*OH and Ir site over Ir₁/TFO. **d** PDOS of Ir₁/TFO. **e** The possible reaction process over Ir₁/TFO photoanode.

coupled with adsorbed OH⁻ to form \*OH, which attacks the C $_{\alpha}$ -H of cyclohexanone to form an enol intermediate<sup>52</sup>. This intermediate is further converted to a 2-hydroxycyclohexanone intermediate via \*OH transfer, which in turn further formed a 2-hydroxycyclohexanone intermediate. \*OH subsequently attacks the C $_{\alpha}$ -H of 2-hydroxycyclohexanone, generating a lactone intermediate, which is hydrolyzed to produce AA<sup>56</sup>.

### Device design for unassisted AA production

Achieving bias-free monolithic system represents a significant objective in the advancement of PEC techniques. Herein, through integration of Ir₁/TFO photoanode and self-designed a-Si photocathode (see detail in Experimental section and Supplementary Figs. 36, 37), we have developed a monolithic PEC system for unassisted light-driven AA production. The operating point corresponds to a potential of 1.6 V vs. RHE (Fig. 6a), enabling simultaneous anodic cyclohexanone oxidation and cathodic water reduction in the system, wherein the light first traverses the unassisted AA production. The overlapped LSV curves of Ir₁/TFO photoanode with cyclohexanone oxidation and typical hydrogen evolution reaction on a-Si photocathode

demonstrate that the device operates effectively at a shared energy level<sup>57</sup>. Figure 6b and Supplementary Fig. 38 provide comprehensive illustration of this unbiased PEC system. Ultimately, the PEC device for unbiased AA production can be operated stably for at least 16 cycles over 80 h, maintaining the FE of AA at  $51.0 \pm 7.6$  % (Fig. 6c).

### Discussion

In summary, we have developed a PEC technique for the selective ring-cleaving oxidation of cyclohexanone to adipic acid (AA) under mild conditions. The Ir₁/TFO photoanode achieved an AA production rate of  $6.0 \mu\text{mol cm}^{-2} \text{h}^{-1}$  with ~60% FE and ~88% selectivity using H₂O as an oxygen source, greatly outperforming conventional TFO photoanode. The charge kinetics analysis indicated Ir single atoms can facilitate photogenerated carrier separation and transfer. Notably, we revealed a non-free-radical reaction mechanism involving \*OH transfer driven by photogenerated holes, distinct from the conventional •OH radical mechanism. DFT calculations confirmed that Ir single atoms regulate the electronic structure of TFO, enabling preferential adsorption of OH⁻ on the single-atom Ir sites, while balancing the competing adsorption of OH⁻ and cyclohexanone on Fe sites. Furthermore, we

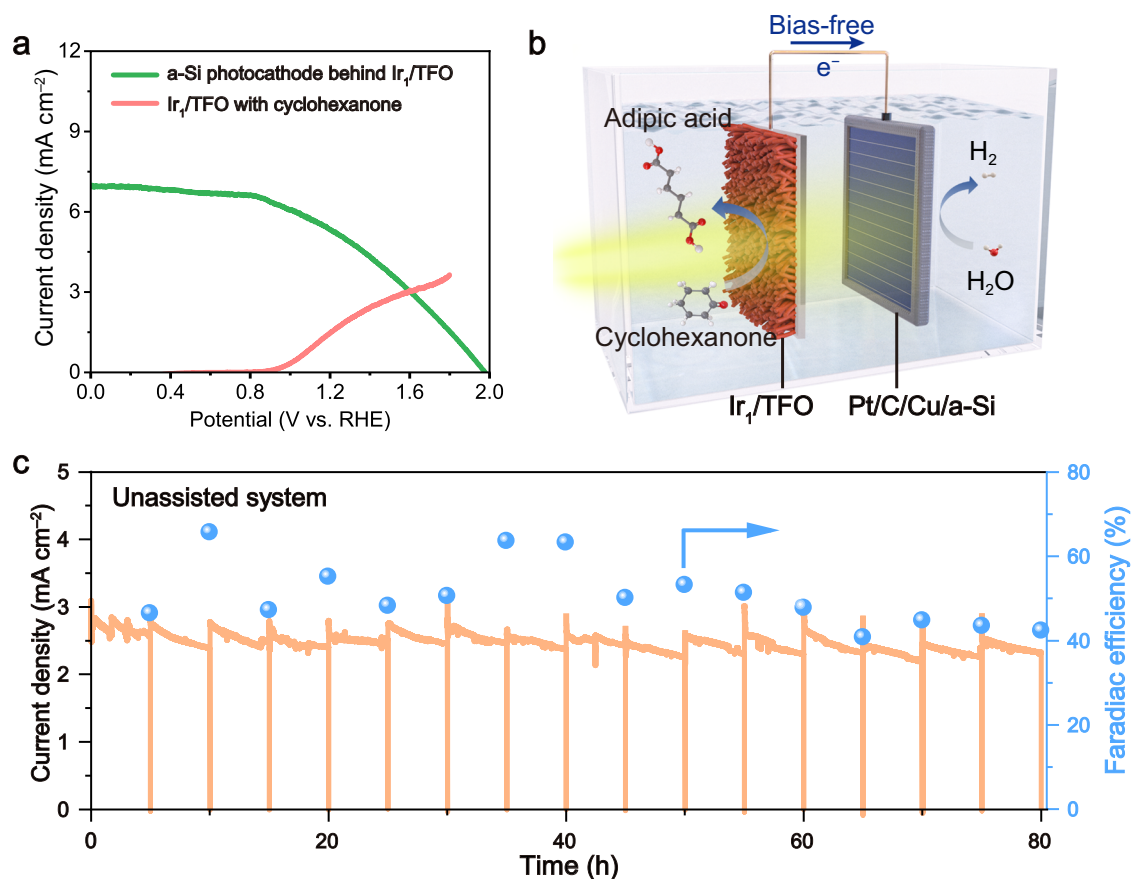


**Fig. 6 | Unassisted device for AA production.** **a** LSV curves of Ir<sub>1</sub>/TFO photoanode and a-Si photocathode behind the Ir<sub>1</sub>/TFO photoanode in 1 M KOH with 20 mM cyclohexanone under AM 1.5 G (100 mWcm<sup>-2</sup>) illumination. **b** Illustration of the

unassisted device for PEC cyclohexanone oxidation coupled with HER. **c** Continuous cycling tests on unassisted device in 1 M KOH with 20 mM cyclohexanone under AM 1.5 G (100 mWcm<sup>-2</sup>) illumination.

demonstrated the feasibility of unassisted PEC device by integrating Ir<sub>1</sub>/TFO photoanode and a-Si photocathode for efficient AA production, achieving stable performance over 80 h. This stable bias-free PEC device underscores the potential of PEC systems for practical applications. Our findings provide a rational design strategy for efficient, selective and sustainable oxidation reactions while offering deep insights into PEC reaction mechanisms at the atomic level.

## Methods

### Preparation of photoanodes

The Ti: Fe<sub>2</sub>O<sub>3</sub> (TFO) photoanode was prepared by a hydrothermal and calcination method. 50 μL TiCl<sub>4</sub> ethanol solution (5 vol. %) was introduced into a 17 mL aqueous solution containing 0.15 M FeCl<sub>3</sub>·3H<sub>2</sub>O, 1 M NaNO<sub>3</sub>, followed by transfer to a Teflon-lined stainless steel autoclave (25 mL) after magnetic stirring for 30 min. Then, the FTO substrate was immersed into the above solution with the conductive side down and heated at 120 °C for 5 h. After cooling to room temperature, a yellow thin film of β-FeOOH nanorods on the FTO substrate can be obtained by washing with deionized water and dried at 60 °C. Finally, the β-FeOOH was calcinated at 750 °C for 20 min to obtain the TFO photoanode.

The Ir<sub>1</sub>/TFO photoanode was prepared by an electrochemical deposition, a method that has been widely used to prepare single-atom electrocatalysts in recent years<sup>58,59</sup>. The deposition was performed in a three-electrode system with a TFO photoanode, a Pt foil, and an Ag/AgCl electrode as the working, counter, and reference electrodes, respectively. Firstly, 5 cycles of LSV from 1.0 to 1.8 V vs. RHE were employed for the pretreatment of TFO electrode in 1 M KOH electrolyte. Afterward, TFO electrode was immersed in an electrolyte containing 50 μM K<sub>2</sub>IrCl<sub>6</sub> and 1 M KOH with continuous stirring for 20 min.

Then electrochemical deposition was performed by scanning the LSV from 1.0 to 1.8 V vs. RHE for 5 cycles with a scan rate of 5 mV s<sup>-1</sup>. Finally, the Ir<sub>1</sub>/TFO photoanode can be obtained by washing with deionized water and dried at 60 °C. Pt<sub>1</sub>/TFO, Pd<sub>1</sub>/TFO and Ru<sub>1</sub>/TFO photoanodes were prepared in the same way as the Ir<sub>1</sub>/TFO photoanode described above, except that K<sub>2</sub>IrCl<sub>6</sub> was replaced with H<sub>2</sub>PtCl<sub>6</sub>, K<sub>2</sub>PdCl<sub>4</sub> and RuCl<sub>3</sub>, respectively.

The IrO<sub>x</sub>/TFO photoanode was prepared by an electrochemical deposition method. The deposition was performed in a three-electrode system with a TFO photoanode, a Pt foil, and an Ag/AgCl electrode as the working, counter, and reference electrodes, respectively. Firstly, 5 cycles of LSV from 1.0 to 1.8 V vs. RHE were employed for the pretreatment of TFO electrode in 1 M KOH electrolyte. Afterward, TFO electrode was immersed in an electrolyte containing 50 μM K<sub>2</sub>IrCl<sub>6</sub> and 1 M KOH with continuous stirring for 20 min. Then electrochemical deposition was performed by cyclic voltammetry (CV) scanning from 1.0 to 1.8 V vs. RHE for 100 cycles with a scan rate of 10 mV s<sup>-1</sup>. Finally, the IrO<sub>x</sub>/TFO photoanode can be obtained by washing with deionized water and dried at 60 °C.

The TiO<sub>2</sub> photoanode was prepared by a hydrothermal and calcination method. Typically, 0.4 mL tetrabutyl titanate was introduced into a 20 mL aqueous solution containing 10 mL HCl (37%) and 10 mL deionized water, followed by transfer to a Teflon-lined stainless steel autoclave (25 mL) after magnetic stirring for 10 min. Then, the FTO substrate was immersed into the above solution with the conductive side down and heated at 150 °C for 8 h. After cooling to room temperature, a white thin film of TiO<sub>2</sub> precursor on the FTO substrate can be obtained by washing with deionized water and dried at 60 °C. Finally, the TiO<sub>2</sub> precursor was calcinated at 500 °C for 2 h to obtain the TiO<sub>2</sub> photoanode.



The Ir<sub>1</sub>/TiO<sub>2</sub> photoanode was prepared in the same way as the Ir<sub>1</sub>/TFO photoanode.

### Photoelectrochemical (PEC) measurements

The PEC measurements were conducted on an electrochemical workstation (CHI 660E, CH Instruments) in a three-electrode system with a photoanode, a Pt foil, and an Ag/AgCl electrode as the working, counter, and reference electrodes, respectively. A 300 W Xe lamp (PLS-SXE300E, Beijing Perfectlight) equipped with AM 1.5 G filter (100 mW cm<sup>-2</sup>) was used as the simulated solar light source. For all PEC measurements, a 1 M KOH electrolyte was consistently employed. The area of illumination was calculated to be 1 cm<sup>2</sup>. LSV experiments were performed by sweeping the potential in the positive direction at a scan rate of 20 mV s<sup>-1</sup>. Transient photocurrent curves were tested with alternating light on/off irradiation each 10 s. Photoelectrochemical impedance spectroscopy (PEIS) measurements were taken by applying an AC voltage amplitude of 5 mV at 1.2 V vs. RHE within the frequency range from 10<sup>5</sup> to 10<sup>-1</sup> Hz under light irradiation. All the potentials reported were converted to RHE scale using the following equation:

$$E(\text{vs. RHE}) = E(\text{vs. Ag/AgCl}) + 0.1976 + 0.0591 \times \text{pH} \quad (1)$$

The applied bias photo-to-current efficiency (ABPE) values were determined using the following equation:

$$\text{ABPE}(\%) = \frac{(1.23 - V_{\text{light}}) \times J}{P} \quad (2)$$

where  $V_{\text{light}}$  is the applied bias potential (vs. RHE),  $J$  is the current density (mA cm<sup>-2</sup>), and  $P$  is the incident light intensity (100 mW cm<sup>-2</sup>).

The open circuit potential (OCP) decay profiles are employed to evaluate the surface recombination between trapped electrons and reaction intermediates, instead of bulk recombination that occurs very fast (nanosecond/microsecond domain). The OCP decay was first stabilized for 50 s under irradiation before the light source was switched off. The carrier lifetimes ( $\tau_B$ ) determined by OCP were calculated using the following formula:

$$\tau_B = \left( \frac{d\text{OCP}}{dt} \right)^{-1} \times \frac{kT}{e} \quad (3)$$

where  $k$  is the Boltzmann's constant ( $1.38 \times 10^{-23}$  J K<sup>-1</sup>),  $T$  is the temperature (K), and  $e$  is the electron charge ( $1.602 \times 10^{-19}$  C).

Charge separation efficiency ( $\eta_{\text{sep}}$ ) and charge injection efficiency ( $\eta_{\text{inj}}$ ) were calculated according to the LSV curves measured in 1 M KOH and 1 M KOH with 0.5 M Na<sub>2</sub>SO<sub>3</sub> electrolytes by the following equations:

$$\eta_{\text{sep}} = \frac{J_{\text{SO}_3^{2-}}}{J_{\text{abs}}} \quad (4)$$

$$\eta_{\text{inj}} = \frac{J_{\text{H}_2\text{O}}}{J_{\text{SO}_3^{2-}}} \quad (5)$$

$$J_{\text{abs}} = \int_{\lambda_1}^{\lambda_2} \frac{\lambda}{1240} P_{\text{abs}}(\lambda) d\lambda \left( \frac{\text{mW}}{\text{cm}^2} \right) \quad (6)$$

where  $J_{\text{abs}}$  is the integrated current density (mA cm<sup>-2</sup>),  $P_{\text{abs}}$  is power of light actually absorbed by photoanode (mW cm<sup>-2</sup> nm<sup>-1</sup>)

### PEC cyclohexanone oxidation measurements

PEC cyclohexanone oxidation measurements were conducted inside a sealed H-type PEC cell. To separate the anode from the cathode chamber, a Nafion 117 proton exchange membrane was employed. The

anode chamber electrolyte solution, which included 1 M KOH and 20 mM cyclohexanone and the cathode chamber electrolyte was filled with 1 M KOH solution. Before the PEC reactions, the solution and the chambers were degassed with Ar for 20 min, then the system was sealed during the reactions. All other experimental conditions were consistent with those utilized for the above PEC measurements. The liquid products could be analyzed by nuclear magnetic resonance (NMR, Bruker AVANCE III 400 MHz) spectrometer. The Faradaic efficiency (FE) and selectivity were calculated using the following equations:

$$\text{FE} = \frac{n \times F}{Q} \times 100\% \quad (7)$$

$$\text{Selectivity} = \frac{n_{\text{AA}}(\text{formation})}{n_{\text{cyclohexanone}}(\text{consumption})} \times 100\% \quad (8)$$

where  $n$  is the molar amount of product,  $F$  is the Faraday's constant (96485 C mol<sup>-1</sup>),  $Q$  is the running Coulomb value.

The incident photon-to-AA conversion efficiency, alternatively termed the quantum efficiency (QE) of AA was calculated using the following equation:

$$\text{QE} = \frac{J_{\text{ph}} \times \frac{hc}{e} \times \text{FE}_{\text{AA}}}{P \times \lambda} \times 100\% \quad (9)$$

where  $J_{\text{ph}}$  is the photo-current density (mA cm<sup>-2</sup>),  $h$  is Planck's constant ( $6.62 \times 10^{-34}$  J s),  $c$  is the speed of light ( $3.0 \times 10^8$  m s<sup>-1</sup>),  $e$  is the electron charge ( $1.602 \times 10^{-19}$  C),  $\text{FE}_{\text{AA}}$  is the Faradaic efficiency of AA,  $P$  is the monochromatic incident light intensity (mW cm<sup>-2</sup>), and  $\lambda$  is the wavelength of monochromatic light (nm).

Unbiased AA production was constructed by integrating an amorphous silicon-based (a-Si) photocathode and an Ir<sub>1</sub>/TFO photoanode in a membrane-free PEC cell, wherein a-Si photocathode was obtained from a commercial amorphous Si stacked solar cell that has been modified with a layer of Cu foil, a conductive carbon paste and a Pt/C co-catalyst.

### DFT calculations

Spin-polarized electronic structure calculations were performed using the plane-wave basis set approach as implemented in the Vienna ab initio simulation package<sup>60</sup>. The projector augmented wave method was used to represent the ion-core electron interactions<sup>61</sup>. The valence electrons were represented with a plane wave basis set with an energy cutoff of 450 eV. Electronic exchange and correlation were described with the Perdew–Burke–Ernzerhof functional<sup>62</sup>. DFT-D3 method was used to treat the van der Waals interaction<sup>63</sup>. A 15 Å vacuum space was included to avoid interactions between surface slabs. A  $3 \times 3 \times 1$  Monkhorst–Pack scheme was used to generate the k-point grid for the modeled surfaces<sup>64</sup>. The convergence criteria for the self-consistent electronic structure and geometry were set to 10<sup>-5</sup> eV and 0.05 eV/Å, respectively. The electronic structure calculations were performed using the spin-dependent GGA plus Hubbard correction U method and the effective  $U_{\text{eff}}$  parameter was set to 5.3 eV.

### Data availability

All data generated in this study are provided in the Source Data file. Source data are provided with this paper.

### References

- Kim, J. H., Hansora, D., Sharma, P., Jang, J.-W. & Lee, J. S. Toward practical solar hydrogen production – an artificial photosynthetic leaf-to-farm challenge. *Chem. Soc. Rev.* **48**, 1908–1971 (2019).
- Andrei, V. et al. Floating perovskite-BiVO<sub>4</sub> devices for scalable solar fuel production. *Nature* **608**, 518–522 (2022).

3. Andrei, V., Roh, I. & Yang, P. Nanowire photochemical diodes for artificial photosynthesis. *Sci. Adv.* **9**, eade9044 (2023).
4. Cha, H. G. & Choi, K.-S. Combined biomass valorization and hydrogen production in a photoelectrochemical cell. *Nat. Chem.* **7**, 328–333 (2015).
5. Chen, Y. et al. Scalable decarboxylative trifluoromethylation by ion-shielding heterogeneous photoelectrocatalysis. *Science* **384**, 670–676 (2024).
6. Zhao, Y. et al.  $\alpha$ -Fe<sub>2</sub>O<sub>3</sub> as a versatile and efficient oxygen atom transfer catalyst in combination with H<sub>2</sub>O as the oxygen source. *Nat. Catal.* **4**, 684–691 (2021).
7. Ren, S., Gao, R. T., Nguyen, N. T. & Wang, L. Enhanced charge carrier dynamics on Sb<sub>2</sub>Se<sub>3</sub> photocathodes for efficient photoelectrochemical nitrate reduction to ammonia. *Angew. Chem. Int. Ed.* **63**, e202317414 (2024).
8. Jiang, C., Moniz, S. J. A., Wang, A., Zhang, T. & Tang, J. Photoelectrochemical devices for solar water splitting – materials and challenges. *Chem. Soc. Rev.* **46**, 4645–4660 (2017).
9. Sendeku, M. G. et al. Frontiers in photoelectrochemical catalysis: a focus on valuable product synthesis. *Adv. Mater.* **36**, 2308101 (2024).
10. Liu, D. et al. Selective photoelectrochemical oxidation of glycerol to high value-added dihydroxyacetone. *Nat. Commun.* **10**, 1779 (2019).
11. Lu, Y. et al. Solar-driven highly selective conversion of glycerol to dihydroxyacetone using surface atom engineered BiVO<sub>4</sub> photoanodes. *Nat. Commun.* **15**, 5475 (2024).
12. Su, K. et al. Bias-free solar-driven ammonia coupled to C<sub>3</sub>-dihydroxyacetone production through photoelectrochemistry. *Angew. Chem. Int. Ed.* **64**, e202422443 (2025).
13. Gao, C. et al. Heterogeneous single-atom photocatalysts: fundamentals and applications. *Chem. Rev.* **120**, 12175–12216 (2020).
14. Si, S. et al. Low-coordination single Au atoms on ultrathin ZnIn<sub>2</sub>S<sub>4</sub> nanosheets for selective photocatalytic CO<sub>2</sub> reduction towards CH<sub>4</sub>. *Angew. Chem. Int. Ed.* **61**, e202209446 (2022).
15. Hu, H. & Xi, J. Single-atom catalysis for organic reactions. *Chin. Chem. Lett.* **34**, 107959 (2023).
16. Liu, D., Wan, X., Kong, T., Han, W. & Xiong, Y. Single-atom-based catalysts for photoelectrocatalysis: challenges and opportunities. *J. Mater. Chem. A* **10**, 5878–5888 (2022).
17. Jun, S. E., Lee, J. K., Ryu, S. & Jang, H. W. Single atom catalysts for photoelectrochemical water splitting. *ChemCatChem* **15**, e202300926 (2023).
18. Liu, T. et al. Low catalyst loading enhances charge accumulation for photoelectrochemical water splitting. *Angew. Chem. Int. Ed.* **62**, e202307909 (2023).
19. Gao, R.-T. et al. Single-atomic-site platinum steers photogenerated charge carrier lifetime of hematite nanoflakes for photoelectrochemical water splitting. *Nat. Commun.* **14**, 2640 (2023).
20. Wu, S.-M. et al. Pt single atoms on TiO<sub>2</sub> can catalyze water oxidation in photoelectrochemical experiments. *J. Am. Chem. Soc.* **146**, 16363–16368 (2024).
21. Tian, Z. et al. Selective photoelectrochemical oxidation of glucose to glucaric acid by single atom Pt decorated defective TiO<sub>2</sub>. *Nat. Commun.* **14**, 142 (2023).
22. Feng, X. et al. Single-atomic-site platinum steers middle hydroxyl selective oxidation on amorphous/crystalline homojunction for photoelectrochemical glycerol oxidation coupled with hydrogen generation. *Adv. Funct. Mater.* **34**, 2316238 (2024).
23. Liu, F. et al. Graphdiyne as an electron modifier for boosting electrochemical production of adipic acid. *Adv. Funct. Mater.* **34**, 2310274 (2023).
24. Hwang, K. C. & Sagadevan, A. One-pot room-temperature conversion of cyclohexane to adipic acid by ozone and UV light. *Science* **346**, 1495–1498 (2014).
25. Hočevar, B., Grilc, M. & Likozar, B. Aqueous dehydration, hydrogenation, and hydrodeoxygenation reactions of bio-based mucic acid over Ni, NiMo, Pt, Rh, and Ru on neutral or acidic catalyst supports. *Catalysts* **9**, 286 (2019).
26. Hočevar, B., Prašnikar, A., Huš, M., Grilc, M. & Likozar, B. H<sub>2</sub>-Free Re-based catalytic dehydroxylation of aldaric acid to muconic and adipic acid esters. *Angew. Chem. Int. Ed.* **60**, 1244–1253 (2020).
27. Teržan, J. et al. Selective oxidation of biomass-derived carbohydrate monomers. *Green. Chem.* **25**, 2220–2240 (2023).
28. Lyalin, B. V. & Petrosyan, V. Electrosynthesis of adipic acid by undivided cell electrolysis. *Russ. Chem. Bull.* **53**, 688–692 (2004).
29. Li, Z. et al. Electrocatalytic synthesis of adipic acid coupled with H<sub>2</sub> production enhanced by a ligand modification strategy. *Nat. Commun.* **13**, 5009 (2022).
30. Cho, I. S., Han, H. S., Logar, M., Park, J. & Zheng, X. Enhancing low-bias performance of hematite photoanodes for solar water splitting by simultaneous reduction of bulk, interface, and surface recombination pathways. *Adv. Energy Mater.* **6**, 1501840 (2015).
31. Malviya, K. D. et al. Influence of Ti doping levels on the photoelectrochemical properties of thin-film hematite ( $\alpha$ -Fe<sub>2</sub>O<sub>3</sub>) photoanodes. *J. Phys. Chem. C* **121**, 4206–4213 (2017).
32. Yi, S. S., Wulan, B. R., Yan, J. M. & Jiang, Q. Highly efficient photoelectrochemical water splitting: surface modification of cobalt-phosphate-loaded Co<sub>3</sub>O<sub>4</sub>/Fe<sub>2</sub>O<sub>3</sub> p–n heterojunction nanorod arrays. *Adv. Funct. Mater.* **29**, 1801902 (2019).
33. Krivanek, O. L. et al. Atom-by-atom structural and chemical analysis by annular dark-field electron microscopy. *Nature* **464**, 571–574 (2010).
34. Lin, Y. et al. Inductive effect of Ti-doping in Fe<sub>2</sub>O<sub>3</sub> enhances the photoelectrochemical water oxidation. *Sci. China Chem.* **66**, 2091–2097 (2023).
35. Zhang, H., Kim, Y. K., Jeong, H. Y. & Lee, J. S. A few atomic FeNbO<sub>4</sub> overlayers on hematite nanorods: microwave-induced high temperature phase for efficient photoelectrochemical water splitting. *ACS Catal.* **9**, 1289–1297 (2018).
36. Wang, J. et al. Engineering the coordination environment of Ir single atoms with surface titanium oxide amorphization for superior chlorine evolution reaction. *J. Am. Chem. Soc.* **146**, 11152–11163 (2024).
37. Wei, J. et al. Optimizing the intermediates adsorption by manipulating the second coordination shell of Ir single atoms for efficient water oxidation. *Angew. Chem. Int. Ed.* **63**, e202410520 (2024).
38. Le Formal, F., Sivula, K. & Grätzel, M. The transient photocurrent and photovoltage behavior of a hematite photoanode under working conditions and the influence of surface treatments. *J. Phys. Chem. C* **116**, 26707–26720 (2012).
39. Yang, T. et al. Interfacial charge transfer bridge prolongs carrier recombination lifetimes of CoFe metal-thiolate framework/hematite photoanode for water oxidation. *Adv. Funct. Mater.* **34**, 2313767 (2024).
40. Tilley, S. D., Cornuz, M., Sivula, K. & Grätzel, M. Light-induced water splitting with hematite: improved nanostructure and iridium oxide catalysis. *Angew. Chem. Int. Ed.* **49**, 6405–6408 (2010).
41. Yuan, S.-Y., Jiang, L.-W., Hu, J.-S., Liu, H. & Wang, J.-J. Fully dispersed IrO<sub>x</sub> atomic clusters enable record photoelectrochemical water oxidation of hematite in acidic media. *Nano Lett.* **23**, 2354–2361 (2023).
42. Lu, Y. et al. Tuning the selective adsorption site of biomass on Co<sub>3</sub>O<sub>4</sub> by Ir single atoms for electrosynthesis. *Adv. Mater.* **33**, 2007056 (2021).
43. Xia, Z. et al. Enhancing the electrocatalytic hydrogenation of furfural via anion-induced molecular activation and adsorption. *J. Am. Chem. Soc.* **146**, 24570–24579 (2024).

44. Fan, Z., Xu, Z., Yan, S. & Zou, Z. Tuning the ion permeability of an  $\text{Al}_2\text{O}_3$  coating layer on  $\text{Fe}_2\text{O}_3$  photoanodes for improved photo-electrochemical water oxidation. *J. Mater. Chem. A* **5**, 8402–8407 (2017).
45. Cesar, I., Sivula, K., Kay, A., Zboril, R. & Grätzel, M. Influence of feature size, film thickness, and silicon doping on the performance of nanostructured hematite photoanodes for solar water splitting. *J. Phys. Chem. C* **113**, 772–782 (2008).
46. Mu, Y. et al. Highly selective electrochemical Baeyer–Villiger oxidation through oxygen atom transfer from water. *J. Am. Chem. Soc.* **146**, 13438–13444 (2024).
47. Dong, J. et al. In situ Raman spectroscopy reveals the structure evolution and lattice oxygen reaction pathway induced by the crystalline–amorphous heterojunction for water oxidation. *Chem. Sci.* **13**, 5639–5649 (2022).
48. Liu, C. et al. Long-term durability of metastable  $\beta\text{-Fe}_2\text{O}_3$  photoanodes in highly corrosive seawater. *Nat. Commun.* **14**, 4266 (2023).
49. Kong, K. et al. Electrochemical carbon–carbon coupling with enhanced activity and racemate stereoselectivity by micro-environment regulation. *Nat. Commun.* **14**, 6925 (2023).
50. Guo, J. et al. Direct seawater electrolysis by adjusting the local reaction environment of a catalyst. *Nat. Energy*, **8**, 264–272 (2023).
51. Jia, Y. et al. Directional electrosynthesis of adipic acid and cyclohexanone by controlling the active sites on  $\text{NiOOH}$ . *J. Am. Chem. Soc.* **146**, 1282–1293 (2023).
52. Liu, X. et al. Electrosynthesis of adipic acid with high faradaic efficiency within a wide potential window. *Nat. Commun.* **15**, 7685 (2024).
53. Li, H. et al. Boosting reactive oxygen species generation using interfacial edge rich  $\text{WO}_3$  arrays for photoelectrochemical conversion. *Angew. Chem. Int. Ed.* **62**, e202210804 (2022).
54. Liu, Y., Shang, H., Zhang, B., Yan, D. & Xiang, X. Surface fluorination of  $\text{BiVO}_4$  for the photoelectrochemical oxidation of glycerol to formic acid. *Nat. Commun.* **15**, 8155 (2024).
55. Xiao, D. et al. Boosting the electrochemical 5-hydroxymethylfurfural oxidation by balancing the competitive adsorption of organic and  $\text{OH}^-$  over controllable reconstructed  $\text{Ni}_3\text{S}_2/\text{NiO}_x$ . *Adv. Mater.* **35**, e2304133 (2023).
56. Rozhko, E. et al. Oxidation of 1,2-Cyclohexanediol to adipic acid with oxygen: a study into selectivity-affecting parameters. *ChemCatChem* **5**, 1998–2008 (2013).
57. Liu, B. et al. Tandem cells for unbiased photoelectrochemical water splitting. *Chem. Soc. Rev.* **52**, 4644–4671 (2023).
58. Zhang, Z. et al. Electrochemical deposition as a universal route for fabricating single-atom catalysts. *Nat. Commun.* **11**, 1215 (2020).
59. Ma, P. et al. Neighbouring synergy in high-density single Ir atoms on  $\text{CoGaOOH}$  for efficient alkaline electrocatalytic oxygen evolution. *Angew. Chem. Int. Ed.* **63**, e202404418 (2024).
60. Kresse, G. & Furthmüller, J. Efficiency of ab-initio total energy calculations for metals and semiconductors using a plane-wave basis set. *Comput. Mater. Sci.* **6**, 15–50 (1996).
61. Kresse, G. & Joubert, D. From ultrasoft pseudopotentials to the projector augmented-wave method. *Phys. Rev. B* **59**, 1758–1775 (1999).
62. Perdew, J. P., Burke, K. & Ernzerhof, M. Generalized gradient approximation made simple. *Phys. Rev. Lett.* **77**, 3865–3868 (1996).
63. Grimme, S., Antony, J., Ehrlich, S. & Krieg, H. A consistent and accurate ab initio parametrization of density functional dispersion correction (DFT-D) for the 94 elements H–Pu. *J. Chem. Phys.* **132**, 154104 (2010).
64. Chadi, D. J. Special points for Brillouin-zone integrations. *Phys. Rev. B* **16**, 1746–1747 (1977).

## Acknowledgements

This work was financially supported by NSFC (22279128 (D.L.), 22172087 (H.C.), 22409189 (J.M.)), West Light Foundation of Chinese Academy of Sciences (xbzg-zdsys-202209 (Y.X.)), Natural Science Foundation of Jiangsu Province (BK20240459 (J.M.)), Suzhou Key Laboratory of Bioinspired Interfacial Science (SZ2024004 (D.L.)). This work was partially carried out at the Instruments Center for Physical Science, University of Science and Technology of China. We thank the support from USTC Center for Micro-and Nanoscale Research and Fabrication, the Supercomputing Center of University of Science and Technology of China, the Physical and Chemical Analysis Center at Suzhou Institute for Advanced Research, University of Science and Technology of China. We also thank the BL01B in the National Synchrotron Radiation Laboratory (NSRL).

## Author contributions

S.S., H.C., D.L. and Y.X. conceived the idea and designed the experiments. S.S. prepared the photoanodes and tested PEC performance. S.S. and Y.M. constructed the unassisted device. S.S., J.M. and W.J. analyzed charge kinetics and DFT calculations. S.S., Y.M., Y.A.L., J.M. and E.D.Z. performed and analyzed in situ spectra. K.S. performed AC-HAADF-STEM and EDS measurements. S.S. wrote the manuscript and H.C., B.H., D.L. and Y.X. revised the manuscript. All the authors contributed to discussions and commented on manuscript.

## Competing interests

The authors declare no competing interests.

## Additional information

**Supplementary information** The online version contains supplementary material available at <https://doi.org/10.1038/s41467-025-60506-w>.

**Correspondence** and requests for materials should be addressed to Hefeng Cheng, Dong Liu or Yujie Xiong.

**Peer review information** *Nature Communications* thanks the anonymous reviewers for their contribution to the peer review of this work. A peer review file is available.

**Reprints and permissions information** is available at <http://www.nature.com/reprints>

**Publisher's note** Springer Nature remains neutral with regard to jurisdictional claims in published maps and institutional affiliations.

**Open Access** This article is licensed under a Creative Commons Attribution-NonCommercial-NoDerivatives 4.0 International License, which permits any non-commercial use, sharing, distribution and reproduction in any medium or format, as long as you give appropriate credit to the original author(s) and the source, provide a link to the Creative Commons licence, and indicate if you modified the licensed material. You do not have permission under this licence to share adapted material derived from this article or parts of it. The images or other third party material in this article are included in the article's Creative Commons licence, unless indicated otherwise in a credit line to the material. If material is not included in the article's Creative Commons licence and your intended use is not permitted by statutory regulation or exceeds the permitted use, you will need to obtain permission directly from the copyright holder. To view a copy of this licence, visit <http://creativecommons.org/licenses/by-nc-nd/4.0/>.

© The Author(s) 2025